# Gravity Inversion Method to Produce Compact and Sharp Images Using $L_0$-norm Constraint with Auto-adaptive Regularization and Combined Stopping Criteria.

Mesay Geletu Gebre [1][*] and Elias Lewi [2]

[1]Wolkite University, College of Natural and Computational Science,

P.O.Box 07, Wolkite, ETHIOPIA, E-mail: mesaygeletu@gmail.com

[2]Addis Ababa University, Institute of Geophysics, Space Science and Astronomy, Addis Ababa, ETHIOPIA

---

[*]Mesay Geletu, Email: mesaygeletu@gmail.com

**Abstract**

We present a gravity inversion method that can produce compact and sharp images, to assist the modeling of non-smooth geologic features. The proposed iterative inversion approach makes use of $L_0$-norm stabilizing functional, hard, and physical parameter inequality constraints, and depth weighting function. The method incorporates an auto-adaptive regularization technique, which automatically determines a suitable regularization parameter and error weighting function that helps to improve both the stability and convergence of the method. The auto-adaptive regularization and error weighting matrix are not dependent on the known noise level. Because of that, the method yields reasonable results even the noise level of the data is not known properly. The utilization of an effectively combined stopping rule to terminate the inversion process is another improvement that is introduced in this work. The capacity and the efficiency of the new inversion method were tested by inverting randomly chosen synthetic and measured data. The synthetic test models consist of multiple causative blocky bodies, with different geometries and density distributions that are vertically and horizontally distributed adjacent to each other. Inversion results of the synthetic data show that the developed method can recover models that adequately match the real geometry, location, and densities of the synthetic causative bodies. Furthermore, the testing of the improved approach using published real gravity data confirmed the potential and practicality of the method in producing compact and sharp inverse images of the subsurface.

*Keywords*— Gravity data, Iterative inversion, $L_0$-norm constraint, Auto-adaptive regularization, Stopping criteria, Compact image.

# 1   Introduction

Gravity measurements have been used in a wide range of geophysical prospecting and investigations, such as in mineral explorations, engineering and environmental problems as well as archeological site investigations (Hinze et al., 2013, p. 20). In general, gravity inversion is a process that is used to determine the density, size, shape, and location of a complex subsurface causative bodies from an observed gravity anomaly, by using different mathematical modeling techniques. Thus, inversion of gravity data constitutes an important step in the quantitative interpretation since the reconstruction of density contrast models markedly increases the amount of information that can be extracted from the gravity data.

However, a principal difficulty with the gravity data inversion is the inherent non-uniqueness and instability that also exists in any geophysical method (Al-Chalabi, 1971; Blakely, 1996, p. 216). In other words, for the given observed gravity data there are many equivalent density distributions that can reproduce the same field data. The standard approach used to select acceptable solutions, that are geologically reasonable, is to use an additional information about the problem by making assumptions on the following aspects: (1) about the model parameters (existing information on the subsurface structure from geological or other geophysical hindsight) and (2) about the data parameters (statistical properties of the inexact data, e.g. Gaussian distribution of errors). Based on these assumptions there are two approaches in gravity inversion: The first approach fixes the density and vary the geometry. This approach is nonlinear in nature and has been studied by many authors, for instance, Lelievre et al. (2015); Camacho et al. (2002) and Camacho et al. (2011). The second approach, which also is the one used in this work, fixes the geometry and vary the density. This approach is linear in nature and has been investigated by many researchers (Li & Oldenburg, 1998; Boulanger & Chouteau, 2001).

In an effort to introduce more qualitative prior information, Last & Kubik (1983) in particular, developed a method called compact gravity inversion. Their strategy utilizes the compactness stabilizer to minimize the area (in 2D) or volume (in 3D) occupied by the causative body, which is equivalent to maximizing its compactness. Barbosa & Silva (1994) generalized the compact inversion method by making use of compactness along several axes using Tikhonov's regularization. In 2006 Silva and Barbosa further developed the Compact inversion method with so-called 'interactive inversion' which estimates the location and geometry of several density anomalies. They simplified their old method (Barbosa & Silva, 1994) to improve computational performance. The generalized compact and interactive inversion strongly need a priori information to yield an accurate estimation.

The compactness stabilizer (Last & Kubik, 1983) also known as the minimum support stabilizer (Port-

59 niaguine & Zhdanov, 1999) has been borrowed and implemented by other researchers in various geo-

60 physical inversion methods (Ajo-Franklin et al., 2007; Stocco et al., 2009; Fei et al., 2018; Feng et al.,

61 2020; Varfinezhad et al., 2020). As it was demonstrated by a number of researchers (Zhdanov & Tol-

62 staya, 2004; Rezaie et al., 2017; Feng et al., 2020; Varfinezhad et al., 2022), this stabilizer is known to

63 yield a compact or focused geophysical model with sharp boundaries. Apart from the inversion methods

64 which produce focused images mentioned above, sparse geophysical inversion approaches derived from

65 $L_p$-norm ($0 \leq p \leq 1$) stabilization have been developed by many researchers. For instance, sparse

66 seismic reflectivity inversion method (Li et al., 2017), direct current resistivity data inversion algorithm

67 (Singh et al., 2018), magnetic data sparse inversion method (Li et al., 2018; Fournier et al., 2020), sparse

68 gravity data inversion technique (Vatankhah et al., 2017; Peng & Liu, 2021), to mention only a few.

69 Some instability of the original compact gravity inversion algorithm of Last & Kubik (1983) was re-

70 ported by Lewi (1997, p. 87) when the data is contaminated with noise. Then Lewi (1997, p. 89)

71 has improved the original compact inversion by introducing a new approach to the 3D compact gravity

72 inversion. The problem with Lewi (1997, p. 89) method arises when dealing with a multiple-source

73 model, where the inversion algorithm tends to concentrate densities towards the surface regardless of

74 the true depth of the causative bodies. In overcoming this drawback, Gebre & Lewi (2022) improved

75 the compact gravity inversion method by incorporating a new depth weighting function. In this paper,

76 we present a gravity inversion method that can produce compact and sharp images, to assist the mod-

77 eling of non-smooth, blocky geologic features with sharp boundaries. The proposed approach is based

78 on the authors previous work (Gebre & Lewi, 2022), to which the reader is referred for further details,

79 with the following two main differences and advancements. The first is proposing and incorporating an

80 auto-adaptive regularization and error weighting function. This has improved the fast convergence of

81 the method while keeping its stability. The second is the implementation of combined stopping criteria

82 to terminate the iteration after an appropriate number of steps.

## 2 Methodology

### 2.1 The 2D model

85 Most fixed geometry gravity inversion algorithms, including the one presented here, employ rectangu-

86 lar prismatic elements, to discretize the subsurface, owing to their flexibility in constructing complex

87 models (Silva & Barbosa, 2006; Commer, 2011; Grandis & Dahrin, 2014). A 2-D model is obtained

88    by discretization of the subsurface under the survey area into a large number of infinitely long hori-

89    zontal rectangular prisms, with the infinitely long dimension oriented in the invariant y-direction, with

90    variations in densities only assumed for the X and Z directions. The 2-D model is illustrated in Fig.

91    1. The density contrasts are constant inside each cell only and can vary individually. Here we have

92    used equal dimension for the cells. However, the algorithm is flexible, to accommodate non-regular

93    size cells. Gravity stations indicted by $\bigtriangledown$ symbols are located at the centers of the upper faces of the

94    rectangular blocks in the top layer. This discretization scheme of the subsurface allows us to calculate

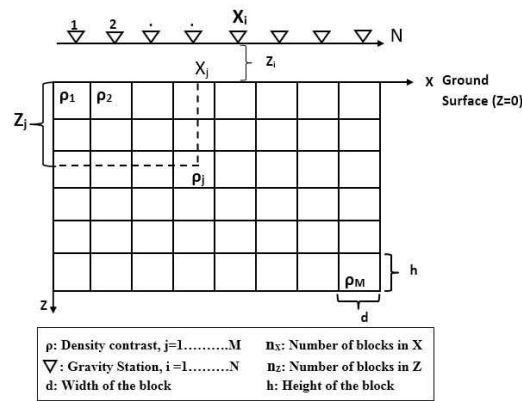the gravitational attraction caused by each rectangular block separately.



Figure 1: A 2-D model of the subsurface under a gravity profile. Gravity stations ($X_i$) are located at the centers of the blocks, indicated by the $\bigtriangledown$ symbols.

95

## 2.2   Forward modelling

97    After discretization of the modeling space into a set of elementary rectangular blocks, the total vertical

98    component gravity response calculated at the $i^{th}$ observation point $g_i$ is the sum of the gravity contribu-

99    tions generated by each of the individual rectangular element, on all points belonging to the observation

100    grid and it is given by:

$$g_i = \sum_{j=1}^{M} a_{ij}\rho_j + e_i \quad i = 1, 2, 3....N \tag{1}$$

101    where $\rho_j$ is the density of the $j^{th}$ prism; $N$ denotes the numbers of observations; $a_{ij}$ is the contribution

102    of $j^{th}$ prism to the gravity value on $i^{th}$ observation point and $e_i$ is the noise associated with $i^{th}$ data point.

103    The kernel $a_{ij}$ is the forward operator that maps from the physical parameter space to the data space.

104    The exact mathematical expression of the kernel used here is presented by Last & Kubik (1983) which

105 is adopted from Nagy (1966) to which the reader is referred for more detail mathematical development.

106 In matrix notation Eq. (1) can be written as:

$$\boldsymbol{g} = \boldsymbol{A}\boldsymbol{\rho} + \boldsymbol{e} \tag{2}$$

107 where $\boldsymbol{g}$ is an N-dimensional vector containing the gravity values, $\boldsymbol{\rho}$ is an M-dimensional model vector

108 of densities, $\boldsymbol{A}$ is the N x M kernel matrix, and $\boldsymbol{e}$ represents the noise vector at data points. Equation

109 (2) constitutes the gravity forward modeling, i.e. used to calculate the predicted gravity anomalies

110 (theoretical data) for a known subsurface density contrast (model $\boldsymbol{\rho}$).

## 2.3 Inverse Modeling

112 Our objective in solving gravity inverse problems is given the observed gravity data ($\boldsymbol{g}$), we seek a

113 solution that gives a density distribution $\boldsymbol{\rho}$ which predicts the observed data with a certain noise level

114 and at the same time, satisfies certain constraints. For the model presented here, the density vector

115 $\boldsymbol{\rho}$ is related to the predicted gravimetric field $\boldsymbol{g}$ by the linear expression given in Eq. (2). Like the

116 majority of practical inverse problems arising in geophysical modeling gravity inversion is an ill-posed

117 problem. Moreover, usually we have less number of the observed gravity data than the number of the

118 model parameters which makes the system under-determined problem. A standard way to solve such

119 ill-posed and under-determined problems, according to regularization theory (Tikhonov et al., 2013), is

120 minimization of the following objective function ($\Phi$) which is the combination of data fidelity or misfit

121 functional ($\Phi_d$) and stabilizing functional (stabilizer) term ($S(\rho)$):

$$\Phi = \Phi_d + \ell^2 S(\rho) \tag{3}$$

122 Here the misfit functional $\Phi_d = \|\boldsymbol{W}_e(\boldsymbol{A}\boldsymbol{\rho} - \boldsymbol{g}^{obs})\|_2^2$, and $\boldsymbol{W}_e$ is error weighting diagonal matrix. In Eq.

123 (3), $\ell$ is a regularization parameter that controls the trade-off between the data fidelity and the stabilizing

124 term. Choosing a small value improves the data fit but the recovered models have highly oscillatory

125 artificial structures (which is equivalent to under-regularization). On the other hand, a large value of $\ell$

126 leads to a large misfit value between the observed and predicted data and a small norm of the model

127 (over-regularizing the solution). Thus, the choice of a suitable value for $\ell$ is very important.

128 The choice of the stabilizing functional, in Eq. (3), depends on the desired model features that are to

129 be recovered. There are several types of stabilizers that have been developed and implemented in the

130  inversion of potential field data, which can roughly be divided into two categories: (I) Smooth stabilizer

131  which uses $L_2$ -norm of the model parameters or gradient of the model parameters (Li & Oldenburg,

132  1998; Cella & Fedi, 2012; Paoletti et al., 2013). (II) Non- smooth stabilizer which uses $L_1$-norm or

133  $L_0$-norm directly on the model parameters or on the gradient of the model parameters (Bertete-Aguirre

134  et al., 2002; Sun & Li, 2014; Li et al., 2018; Utsugi, 2019). Inversion methods that utilize a smooth stabi-

135  lizer produce model typically characterized by smooth features, and hence have difficulties in recovering

136  blocky structures or non-smooth distributions that have sharp boundaries or abrupt changes in physical

137  properties (Farquharson, 2008). To overcome this problem, non-smooth stabilizers that help to produce

138  compact and sharp models have been applied successfully (Zhdanov, 2009; Meng et al., 2018). Since

139  we are interested in developing a gravity inversion method that can produce compact and sharp models,

140  we use a non-smooth stabilizer through the $L_0$-norm on the model parameters and will be discussed in

141  the next subsection.

142  Minimizing the objective function $\Phi$ in Eq. (3), using the standard weighted-damped least-square opti-

143  mization, the estimated density distribution in matrix notation can be given by (Menke, 1989, p. 55):

$$\rho^{k+1} = \rho_F^k + \left[ [\boldsymbol{W}_c^k]^{-1} \boldsymbol{A}^T \left( \boldsymbol{A}[\boldsymbol{W}_c^k]^{-1} \boldsymbol{A}^T + \ell^2 [\boldsymbol{W}_e^k]^{-1} \right)^{-1} \boldsymbol{g}_r^k \right] \tag{4}$$

145  where the superscript $k$ denotes that variable at $k^{th}$ iteration and $\boldsymbol{W}_c^k$ is a combined weighting matrix.

146  $\rho_F^k$ is reference density vector, which is from prior information or calculated at each iteration. $\boldsymbol{g}_r^k =$

147  $\boldsymbol{g}^{obs} - \boldsymbol{A}\rho_F^k$ represents residual data vector computed at each iteration. Computation of the regularization

148  parameter $\ell$ in Eq. (4) will be described in Sect. 2.3.3. In this work, the combined weighting matrix

149  $(\boldsymbol{W}_c^k)$ is defined as a product of three different diagonal matrices, $L_0$-norm constraint matrix $(\boldsymbol{W}_{L_0}^k)$,

150  depth weighting $(\boldsymbol{W}_z)$ and hard constraint matrix $(\boldsymbol{W}_h^k)$.

$$\boldsymbol{W}_c^k = \boldsymbol{W}_{L_0}^k \boldsymbol{W}_z \boldsymbol{W}_h^k \tag{5}$$

### 151  2.3.1  $L_0$-norm Constraint

152  The $L_0$-norm is commonly defined as the number of nonzero elements in a vector. Because there is no

153  analytical formula that meets the mathematical requirement to be regarded as $L_0$-norm, the approximate

154  expression is usually used to convert the $L_0$-norm into an equivalent norm for the suitability of computa-

155  tion. In literature (Zhao et al., 2016; Li & Yao, 2020) that discusses the inversion of potential field data,

156    different L$_0$-norm approximate stabilization functions have been developed and implemented to obtain

157    focused images and sharp boundaries. Meng (2016) used a hyperbolic tangent function to approximate

158    the L$_0$-norm and applied it for 3D inversion of gravity gradient tensor data. Meng et al. (2018) proposed

159    an exponential mathematical function to approximate the L$_0$-norm for 3D gravity sparse inversion. In

160    this paper, the minimum support functional, which is also called compactness constraint originally pro-

161    posed by Last & Kubik (1983) and then further extended by Portniaguine & Zhdanov (1999) to include

162    a reference model is selected which can be expressed as follows:

$$S(\rho) = \sum_{j=1}^{M} \frac{(\rho_j - \rho_j^{apr})^2}{(\rho_j - \rho_j^{apr})^2 + \varepsilon} \tag{6}$$

163    In our case to avoid the requirement of a prior model, we set $\boldsymbol{\rho}_j^{apr} = 0$. Using the function in Eq. (6)

164    as stabilizing functional in the objective function ($\Phi$) is equivalent to using L$_0$-norm based stabilization

165    and thus it can be rewritten as follows (Sun & Li, 2014):

$$L_0(\rho) = \sum_{j=1}^{M} \frac{\rho_j^2}{\rho_j^2 + \varepsilon} \tag{7}$$

166    where $\varepsilon$ is a focusing parameter. Application of $L_0(\rho)$ as stabilizer in minimization process of the

167    objective function (Eq. (3)) leads to the following choice of an L$_0$-norm constraint $W_{L_0}$ which is given

168    by (Last & Kubik, 1983):

$$[W_{L_0}]_j = ([\rho_j]^2 + \varepsilon)^{-1} \tag{8}$$

169    Based on Eq. (8) the $k^{th}$ iteration diagonal elements of the L$_0$-norm constraint matrix ($\boldsymbol{W}_{L_0}^k$) can be

170    formulated as follows:

$$[\boldsymbol{W}_{L_0}^k]_{jj}^{-1} = [\rho_j{}^{k-1}]^2 + \varepsilon \tag{9}$$

171    The focusing parameter $\varepsilon$ is a very important parameter. Its main purpose is to avoid singularities when

172    $\rho_j \rightarrow 0$. The parameter $\varepsilon$ is a small number and in general, we are interested in the case where $\varepsilon \rightarrow 0$

173    because a small value leads to very compact models. However, this may introduce instability. On the

174    other hand, if $\varepsilon$ is chosen large the L$_0$-norm compactness constraint has no influence on the compactness

175    of the model that means it results in a smooth solution. Figure 2 shows the comparison of the minimum

176    support stabilizing functional for different values of $\varepsilon$ to demonstrate the impact of the choice different

177    values of $\varepsilon$ further. From Fig. 2, one can see that as $\varepsilon$ becomes large the minimum support stabilizing

178    function loses its property and behaves more like the minimum length L$_2$-norm stabilizer which results

179 in undesirable smoothness in the model though it improves the stability. Therefore, it is very essential
to choose an optimal value of $\varepsilon$.
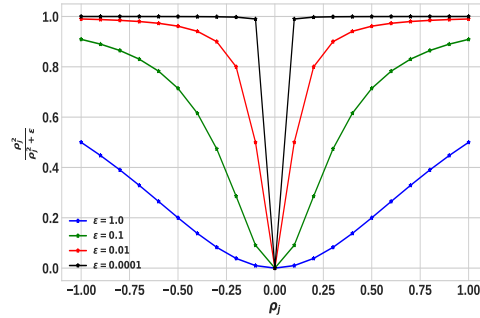


Figure 2: Comparison of the minimum support stabilizing function for different values of $\varepsilon$.

180

181 In previous investigations e.g Last & Kubik (1983) and Guillen & Menichetti (1984) the parameter $\varepsilon$

182 was assigned a value close to machine precision ($\approx 10^{-11} \quad to \quad 10^{-15}$). Alternatively, Zhdanov &

183 Tolstaya (2004) introduced a trade-off curve method, similar to the L-curve technique, to select $\varepsilon$ by

184 computing the model objective for the current model estimate over a range of values for $\varepsilon$. However,

185 as pointed out by Ajo-Franklin et al. (2007) setting $\varepsilon$ to values near machine precision results in severe

186 instability as $\rho_j \rightarrow 0$ and the approach of Zhdanov & Tolstaya (2004) often yields trade-off curves with

187 corners that are not well defined. Therefore it is better to fix $\varepsilon$ at a reasonable value determined by

188 experience, typically between $10^{-4} \quad to \quad 10^{-7}$ (Ajo-Franklin et al., 2007). Accordingly, in the present

189 work based on several numerical simulation tests, the value $10^{-6}$ is assigned just for the inversion

190 examples presented in the manuscript. Note that the developed method is flexible to use different values

191 of $\varepsilon$.

### 2.3.2 Error weighting

193 According to compact inversion method proposed by Last & Kubik (1983), the $k^{th}$ iteration error weight-

194 ing matrix $\boldsymbol{W_e^k}$ is defined as:

$$[\boldsymbol{W_e^k}]^{-1} = diag\left(\boldsymbol{A}[\boldsymbol{W_{L_0}^k}]^{-1}\boldsymbol{A}^T\right) \tag{10}$$

195 Even though $\boldsymbol{W_e^k}$ expressed by Eq. (10) is applied by many authors (Guillen & Menichetti, 1984;

196 Barbosa & Silva, 1994; Ghalehnoee et al., 2017; Gebre & Lewi, 2022), some instability was reported

9

197  by Lewi (1997, p. 87) in using $\boldsymbol{W}_e^k$ in scenarios such as complicated geological geometry and when

198  the data is contaminated with noise. To overcome this problem Lewi (1997, p. 90) proposed to use a

199  weighting matrix that make use of the following equation:

$$[\boldsymbol{W}_e^k]^{-1} = \left[ \frac{[\sigma_\rho^2]^k}{1 + [\sigma_e^2]^k} \right] \boldsymbol{I} \tag{11}$$

200  where $\boldsymbol{I}$ represents identity matrix, and $\sigma_\rho^2$ and $\sigma_e^2$ are model and error variances respectively that are

201  given by:

$$[\sigma_e^2]^k = \frac{\sum_{i=1}^N \{\boldsymbol{g_i} - \sum_{j=1}^M a_{ij}[\boldsymbol{\rho}_j{}^{k-1}]\}^2}{N - 1} \tag{12}$$

203

$$[\sigma_\rho^2]^k = \frac{\sum_{j=1}^M [\boldsymbol{\rho}_j{}^{k-1}]^2}{M - 1} \tag{13}$$

205  The term in square brackets in Eq. (11) can be considered as regularization parameter (Silva & Barbosa,

206  2006; Lewi, 1997, p. 90). Based on several numerical experiments done in the present work it was

207  observed that this term can sometimes ends up in a larger value which may result over-regularization of

208  the solution. For this reason, in the present study a new error weighting matrix $\boldsymbol{W}_{ne}^k$ is introduced and

209  it is given as:

$$[\boldsymbol{W}_{ne}^k]^{-1} = diag \left( \boldsymbol{A} \left[ \boldsymbol{W}_z(\frac{[\sigma_\rho^2]^k}{1 + [\sigma_e^2]^k})\boldsymbol{W}_h^k \right] \boldsymbol{A}^T \right) \tag{14}$$

211  Let us represent the terms in square brackets by $\boldsymbol{W}_n^k$ as follows:

$$\boldsymbol{W}_n^k = \boldsymbol{W}_z \left( \frac{[\sigma_\rho^2]^k}{1 + [\sigma_e^2]^k} \right) \boldsymbol{W}_h^k \tag{15}$$

213  where $\boldsymbol{W_z}$ and $\boldsymbol{W}_h^k$ are diagonal depth and hard constraint matrices respectively and will be described in

214  the next subsections. Then the error weighting matrix in Eq. (14), the one introduced and implemented

215  here becomes:

$$[\boldsymbol{W_{ne}^k}]^{-1} = diag \left( \boldsymbol{A}\boldsymbol{W}_n^k\boldsymbol{A}^T \right) \tag{16}$$

### 2.3.3 Auto-adaptive Regularization Parameter Estimation

217  Choosing a suitable value for regularization parameter is a crucial part of the inversion process. The

218  precise value of regularization parameter depends on the noise level associated with the observed data.

219  Thus, the higher value of $\ell$ refers to the higher noise level of the data points. Several methods have been

220  proposed to choose the appropriate value of regularization parameters, and are reviewed in the literature

221 (Farquharson & Oldenburg, 2004; Vatankhah et al., 2014) and standard texts for example Vogel (2002,

222 pp. 97-109) and Aster et al. (2018, p. 57). Particularly, depending on the noise level a constant value

223 of $\ell$, throughout the inversion, has been chosen by many authors (Silva & Barbosa, 2006; Ghalehnoee

224 et al., 2017). In other works, for example Zhdanov (2009) and Rezaie et al. (2017) the parameter $\ell$ has

225 been iteratively updated in each iteration.

226 As pointed out in previous works (Farquharson & Oldenburg, 2004; Gholami & Aghamiry, 2017) in-

227 stead of using a constant value of $\ell$, dynamic re-adjustment throughout the iterative scheme might be

228 a superior approach. Taking this into account, in the present work $\ell$ is updated in each iterative step.

229 In our implementation, to select an optimal regularization parameter at each iteration, we proposed an

230 auto-adaptive regularization method. This method leads to an automatic update of the regularization

231 parameter at each and every iteration. The basic principle including its procedure in relation to formally

232 known adaptive regularization approach which was proposed by Zhdanov (2002, p. 55) and implemented

233 by many authors (Zhdanov, 2009; Rezaie et al., 2017) is as follows. In adaptive regularization approach

234 the initial value of the regularization parameter $\ell^1$ is updated at each iteration step by (Zhdanov, 2002,

235 p. 55):

$$\ell^k = \ell^1 q^k \tag{17}$$

236 where $q$, as described by Zhdanov (2002, p. 55), is damping factor which decreases from iteration to

237 iteration. Its initial value is empirically determined having a value between zero and one. It is obvious

238 that the trial and error selection of the value for $q$ requires computational work . The presented auto-

239 adaptive regularization method overcomes this problem and the iterative values $\ell^k$ are determined by the

240 following formula:

$$\ell^k = \ell^{k-1} \left[ \frac{|\boldsymbol{g} - \boldsymbol{A\rho}|_{max}^{k-1}}{|\boldsymbol{g} - \boldsymbol{A\rho}|_{max}^{k}} \right] \tag{18}$$

241 where the term in the square bracket is an adjusting factor that is automatically determined at each

242 iterative step. In the auto-adaptive regularization method, choosing a suitable initial value of $(\ell_o)$ is

243 essential. Based on a number of synthetic and real data simulations done in this work we recommend

244 the following in choosing a reasonable value of $\ell_o$: Firstly, the initial value of $\ell$ should be within the

245 range $0 < \ell_o \leq 1$. Secondly the precise value of $\ell_o$ depends on the noise level related with the observed

246 data. When the probable or expected noise level of the data is higher, a larger value $\ell_o$ is a reasonable

247 choice to avoid unwanted and false anomalies due to noise. In contrast, when the probable or expected

248 noise level is less a small value of $\ell_o$ should be chosen. Once an appropriate initial value $\ell_o$ is given as an

11

249    input, then for subsequent iterations Eq. (18) is used to determine $\ell^k$. The advantage of the auto-adaptive

250    regularization scheme is its capability to automatically determine a suitable regularization parameter, in

251    the course of the optimization process, depending on the automatically determined adjusting factor.

### 2.3.4   Physical Parameter Inequality Constraint

253    To produce a physically meaningful model from a gravity inverse solution, the usage of lower and upper

254    bound constraints on the recovered density contrast is beneficial (Silva et al., 2001; Grandis & Dahrin,

255    2014). Lower and upper bounds can be obtained from a prior information such as geological investiga-

256    tions in conjunction with published density values of rocks, well-logging, and/or laboratory tests. Many

257    procedures such as gradient projection approach (Wang & Ma, 2007; Lelièvre et al., 2009), transform

258    function approach (Pilkington, 2008) and logarithmic barrier approach (Li & Oldenburg, 2003) have

259    been applied in different inversion schemes to implement this constraint. However, with regard to $L_0$-

260    norm stabilizer based gravity inversion methods an effective method is the direct utilization of lower

261    and upper density constraint (Meng et al., 2018). Hence, in this work the direct density bound inequal-

262    ity constraint is used, that is at each iteration density contrast of each rectangular block is bounded by

263    minimum and maximum density constraint function given by:

264

$$
\begin{aligned}
&if \quad [\boldsymbol{\rho}^k]_j > [\boldsymbol{\rho}_{max}]_j \\
&if \quad [\boldsymbol{\rho}_{min}]_j < [\boldsymbol{\rho}^k]_j < [\boldsymbol{\rho}_{max}]_j \\
&if \quad [\boldsymbol{\rho}^k]_j < [\boldsymbol{\rho}_{min}]_j
\end{aligned}
\quad
\begin{cases}
[\boldsymbol{\rho}^k]_j = [\boldsymbol{\rho}_{max}]_j \\
[\boldsymbol{\rho}^k]_j = [\boldsymbol{\rho}^k]_j \\
[\boldsymbol{\rho}^k]_j = [\boldsymbol{\rho}_{min}]_j
\end{cases}
\tag{19}
$$

265    By using this function, if $k^{th}$ iteration $\rho_j$ of any block exceeds one of its bounds, then it will be fixed at

266    the violated bound.

267    In each iteration step the procedure to compute the hard constraint matrix $\boldsymbol{W}_h^k$ (Boulanger & Chouteau,

268    2001) and the reference density vector $\boldsymbol{\rho}_F^k$ is determined as follows: The diagonal elements of $\boldsymbol{W}_h^k$ are

269    fixed at $\varepsilon$ or 1.0. When a prior geological and geophysical information are able to provide the initial

270    value of density contrast of the $j^{th}$ specific cells, then these values are assigned to the corresponding

271    $[\boldsymbol{\rho}_F^k]_j$. Simultaneously, the corresponding diagonal elements of $[\boldsymbol{W}_h^k]_{jj}$ are set to be $\varepsilon$. During the in-

272    version process, if the $j^{th}$ elements of estimated density values falls out of inequality constraint limits

273    defined by $\rho_{min}$ and $\rho_{max}$, then $[\boldsymbol{\rho}_F^k]_j$ will be fixed at the violated bound density itself and $[\boldsymbol{W}_h^k]_{jj}$

274    assigned to be $\varepsilon$. On the other hand, if the elements of the estimated density did not exceed its bounds

275    (i.e. lies between the limits), $[\boldsymbol{W}_h^k]_{jj}$ and $[\boldsymbol{\rho}_F^k]_j$ are assigned to be 1.0 and 0.0 respectively.

276  Using $\boldsymbol{W}_h^k$ any blocks whose density is known from a priori information or exceeds the density con-

277  straint limit, the algorithm will automatically freezes this block in the next iteration by assigning a very

278  small weight to it. Whereas, $\boldsymbol{\rho}_F^k$ is used to remove the gravity effects of those cells that have crossed

279  the inequality constraint limit from the observed gravity data. That is applied to compute the reduced

280  gravity data vector $\boldsymbol{g}_r^k = \boldsymbol{g}^{obs} - \boldsymbol{A}\boldsymbol{\rho}_F^k$ in Eq. (4) of the inversion algorithm. In other word, at each

281  iterative step the inversion of subsequent iteration will be performed using reduced gravity data vector.

### 2.3.5  Depth weighting

283  It is well known that gravity data, like any potential field data, has no inherent depth resolution. The

284  reconstructed model structures by the inversion process tend to concentrate near the surface regardless of

285  the true depth of the causative bodies (Li & Oldenburg, 1996). This happens because the inverse solution

286  of model construction is a linear combination of kernel, whose amplitudes rapidly decay with depth. The

287  problem can be overcome by introducing a depth weighting matrix to counteract the natural decay of

288  kernel with depth (Li & Oldenburg, 1998). Depth weighting is designed to ensure that all cells have

289  equal likelihood to accommodate the sources, not just those at shallow levels that are most sensitive to

290  the observed data. Depth weighting is used and its effect is investigated by different authors (Pilkington,

291  2008; Commer, 2011). Based on Gebre & Lewi (2022), the recently proposed depth weighting function

292  is given as follows:

$$w_{zj} = (aZ_j + c_o)^{-\tau} \tag{20}$$

294  where $Z_j$ is the mean depth of the $j^{th}$ cell and $a$, $c_o$ and $\tau$ are adjustable parameters. The values of

295  the three adjustable parameters are computed by optimizing $w_z(z)$ to match with the actual gravity

296  kernel values utilizing nonlinear least-squares minimization (Virtanen et al., 2020). Accordingly, for all

297  inversions in this work the depth weighting matrix similar to the one used by Gebre & Lewi (2022) is

298  employed (Eq. (21)):

$$[\boldsymbol{W_z}]_{jj} = \boldsymbol{diag}(w_{zj}) \tag{21}$$

300  where $\boldsymbol{W}_z$ is diagonal M x M depth weighting matrix.

### 2.3.6  Stopping Criteria

302  It is clear that if the iterations are stopped too early, then a reasonable solution of the inverse problem may

303  not be obtained. On the other hand, too many iterations may waste computer time without increasing the

13

304　overall solution qualities. Thus, an important aspect of any iterative inversion method is to decide when

305　the iterations should be terminated. A number of stopping criteria have been proposed and employed to

306　terminate iterative inversion algorithms (Borges et al., 2015; Levin & Meltzer, 2017). Commonly used

307　stopping criteria are based on a norm of the residual vector (i.e. the norm of the difference between

308　estimated and observed data). For instance, a noise level, i.e. $\chi^2 = ||\boldsymbol{W}_d(\boldsymbol{g}^{obs} - \boldsymbol{A}\boldsymbol{\rho})||_2^2$, where a

309　diagonal data weighting matrix $\boldsymbol{W}_d$, whose $i^{th}$ element is the inverse of the standard deviation of the

310　noise at each data point, is used by Boulanger & Chouteau (2001) and Vatankhah et al. (2017). Other

311　criteria for stopping gravity inversion procedure are based on simple $misfit$ or the Root Mean Square

312　Error ($RMSE$) between the observed data and predicted data produced by the recovered model (see, for

313　example Rezaie & Moazam (2017)). The expressions used to estimate these criteria are the following:

$$314 \qquad misfit = \left( \frac{\sum_{i=1}^{N}(\boldsymbol{g}_i^{obs} - \boldsymbol{g}_i^{cal})^2}{\sum_{i=1}^{N}(\boldsymbol{g}_i^{obs})^2} \right)^{\frac{1}{2}} \qquad (22)$$

315

$$316 \qquad RMSE = \frac{(\sum_{i=1}^{N}(\boldsymbol{g}_i^{obs} - \boldsymbol{g}_i^{cal})^2)^{\frac{1}{2}}}{N} \qquad (23)$$

317　Ekinci (2008) also introduced other possible criterion, namely the parameter variation function ($smy$)

318　which is defined as:

$$319 \qquad smy = \left( \sum_{j=1}^{M}(\boldsymbol{\rho}_j{}^{k} - \boldsymbol{\rho}_j{}^{k-1})^2 \right)^{\frac{1}{2}} \qquad (24)$$

320

321　The most widely used approach is to quit the iterative process when one of the above criteria are below

322　a given tolerance (the level of observational error). However, in practical applications a precise value

323　for such tolerance is rarely known; rather, only some possibly vague idea of the desired quality of

324　the numerical approximation is at hand. Moreover, it has been pointed out by Rao et al. (2018) that

325　stopping iteration based solely on the norm of the residual is neither safe nor a robust solution. The

326　non-uniqueness and instability of the gravity inverse problem further complicates the usage of only

327　one of the aforementioned stopping criteria. To overcome these issues, a combination of the $misfit$

328　and $smy$ has been utilized in this paper. Therefore, the iterative procedure continues until one of the

329　following stopping criteria is met: (I) the maximum number of iteration ($k_{max}$) given by the user is

330　reached or (II) the difference between two consecutive iteration values of $smy$ and $misfit$ have reached

331　the target values. That means for the second criterion both the conditions $|smy^{k-1} - smy^k| \leq \tau$ and

332　$|misfit^{k-1} - misfit^k| \leq \mu$ must be satisfied at the same time. In all demonstrations considered in this

333   work, after testing different values, the parameter $\tau$ is assigned to $\sqrt{2M}$; and $\mu$ to 0.005. Where M is

334   again the total number of model parameter. The effectiveness of the proposed termination criteria will

335   be illustrated by using synthetic tests.

## 2.4   Computational procedure

337   The solution of the linear system of equations in Eq. (2) will be carried iteratively using the information

338   about the misfit and density from successive iteration. The input parameters for the inversion proce-

339   dure are: (1) Kernel matrix ($\boldsymbol{A}$) and discretized subsurface model (mesh) and its initial approximation

340   reference density model $\boldsymbol{\rho}_F$ if exits based on a priori information; (2) Observed gravity anomaly ($\boldsymbol{g}$)

341   at measurement points (**x**); (3) Maximum number of iteration ($k_{max}$) and the constant $\beta$; (4) Lower

342   $\boldsymbol{\rho}_{min}$ and upper $\boldsymbol{\rho}_{max}$ density bounds and initial $\ell_o$ value. In summary, the steps taken to carry out the

343   inversion process consists the followings.

344   1. For k = 0, if there is no a priori information, $\boldsymbol{W}_{L_0}$, $\boldsymbol{W}_c$, $\boldsymbol{W}_n$ and $\boldsymbol{W}_h$ are identity matrices,

345      $\boldsymbol{\rho}_F = 0$. $\boldsymbol{W}_z$ and $\boldsymbol{W}_{ne}$ are computed through Eq. (21) and (16) respectively, after this, the first

346      iteration model parameter solution is obtained by Eq. (4).

347   2. The elements of $\boldsymbol{W}_h$ and $\boldsymbol{\rho}_F$ are updated as explained in preceding section, then $\boldsymbol{W}_{L_0}$ is calcu-

348      lated using Eq. (9) and then $\boldsymbol{W}_c$ using Eq. (5).

349   3. Compute the value of $\sigma_\rho$ and $\sigma_e$ using expressions (13) and (12) respectively. Then calculate $\boldsymbol{W}_n$

350      using Eq. (15).

351   4. To remove the effect of those blocks that have crossed the maximum target density, evaluate the

352      reduced data $\boldsymbol{g}_r^k = \boldsymbol{g}^{obs} - \boldsymbol{A}\boldsymbol{\rho}_F^k$. Then compute the current $\ell$ with Eq. (18) and $\boldsymbol{W}_{ne}$ with Eq.

353      (16).

354   5. Carrying out the inversion through Eq. (4).

355   6. Application of bounded constraints on density are carried out as discussed in the preceding sec-

356      tion.

357   7. Now a forward modelling procedure will be carried out using Eq. (2) to compute the gravity

358      anomaly $\boldsymbol{g}^{cal}$ from the estimated model in the previous iteration.

15

8. Data $misfit$ (Eq. (22)) and $smy$ (Eq. (24)) are computed using $\boldsymbol{g^{cal}}$ from step 7, and obtained
   model parameters from the previous and current iteration.

9. Test if the stopping criteria are fulfilled. If the termination criteria are satisfied the iteration
   terminates and obtained results are stored and plotted. Otherwise, using the current estimated
   density model, move to the next iteration k by going to the second step and continue the iterative
   procedure until the stopping criteria are fulfilled.

# 3   Synthetic Model Test

To evaluate the functionality and efficiency of the method, the developed procedure was tested on several synthetic model examples. The examples presented here are randomly chosen to demonstrate: (I) the applicability of the proposed auto-adaptive regularization technique (Eq. (18)) and error weighting function (Eq. (16)); (II) the performance of the method in producing compact and sharp images of the causative bodies; (III) the effectiveness of the combined stopping criterion. The forward and the inverse problem were carried out using the procedure described in the preceding sections. In the inversion of the synthetic examples, the same subsurface discretization as the one used in generating the synthetic data (Forward modeling) is used. All the inversion tests are performed on a Desktop computer ( $11^{th}$ Gen Intel(R) Core(TM) i7-11700, 2.50GHz processor). For the first and second synthetic examples presented in this work: (I) The model region was discretized into 60 x 15 rectangular cells and the dimensions of each cell were taken as 10 x 10 m, in the X and Y directions respectively. (II) The synthetic gravity data were computed at 60 data points that are centered in each cell at the top side of the model, to produce data at 10 m sample interval. (III) The computed gravity anomalies are contaminated with Gaussian noise that has a standard deviation that amounts to 4 % of the magnitude at each data point with zero mean (Farquharson, 2008; Rezaie et al., 2017).

The first synthetic data inversion has been done for the model presented in Fig. 3(a). For this synthetic model the causative bodies are two rectangular structures elongated differently in the horizontal and vertical directions and located at different depths. The causative bodies have the same density contrast $1000 \ kg/m^3$. The density of the causative bodies are given relative to the zero density of uniform background. Figure 3(a) upper panel shows noise free (solid line) and noise contaminated (star dots) gravity data. Separate inversion runs, for three different $\ell_o$ values ( 0.2, 0.3 and 0.4 ), were performed with the developed inversion method. Note that, for subsequent iterations the proposed auto-adaptive regular-

16

388  ization technique (Eq. (18)) is used to compute $\ell$ for each case. At the beginning of the inversion, the

389  iterations are initialized with $\boldsymbol{\rho}_F = 0$ and $\boldsymbol{W}_h = \boldsymbol{W}_c = \boldsymbol{W}_n = \boldsymbol{W}_{L_0} = \boldsymbol{I}$. The lower limit density

contrasts of all cells is zero ($\boldsymbol{\rho}_{min} = 0$) and the upper bound $\boldsymbol{\rho}_{max} = 1000 \; kg/m^3$.
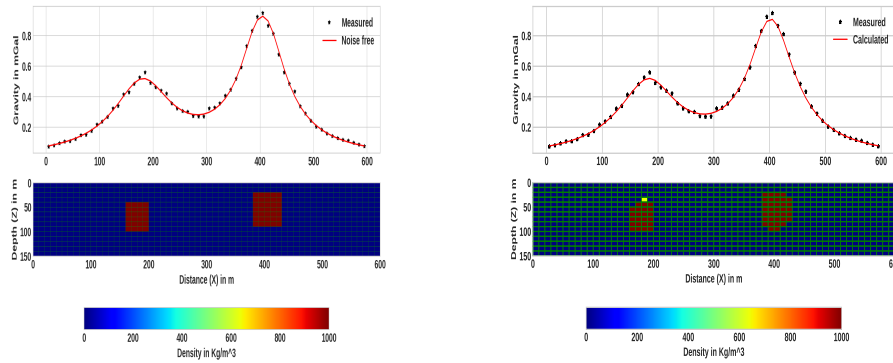


(a) The lower panel represents 2-D synthetic model, which constitutes two isolated rectangular bodies located at various depths and the top panel shows the gravity anomaly due to these two subsurface rectangular bodies.

(b) The lower panel represents the subsurface, as a result of the proposed inversion method using $\ell_o = 0.3$ and the top panel shows the synthetic data together data derived from the model.

Figure 3: The first synthetic model and the result of the inversion.

390

391  The results of the inversion by using the developed method for three different $\ell_o$ values are shown in

392  Figs. 3(b) and 4. The corresponding data fit between the predicted gravity anomaly (solid line ) and

393  actual contaminated data (stars) are also shown. Comparing the inversion results with the original syn-

394  thetic model in Fig. 3(a), the inversion has sufficiently recovered the true models. The depth, geometry,

395  and density distributions of the synthetic causative bodies were recovered adequately. This can confirm

396  the applicability of the proposed auto-adaptive regularization technique (Eq. (18)) and error weighting

397  function (Eq. (16)). Notice that the results also indicate the robustness and stability of the developed

398  inversion method for different $\ell_o$ values. The avarge computation time to finish the inversion is approx-

399  imately 16.3 seconds.

400  The second synthetic model is more complicated and consists of two causative bodies placed at various

401  depth. The bodies have different sizes, shapes, and density contrasts. The first causative body is a verti-

402  cal rectangular block, with density contrast 2000 $kg/m^3$, placed at 40 m depth and the second body is

403  a dipping dike with density contrast 3000 $kg/m^3$ at 20 m depth. The synthetic model is shown in the

404  lower part of Fig. 5(a) and the generated noise-corrupted and noise free gravity data are shown on the
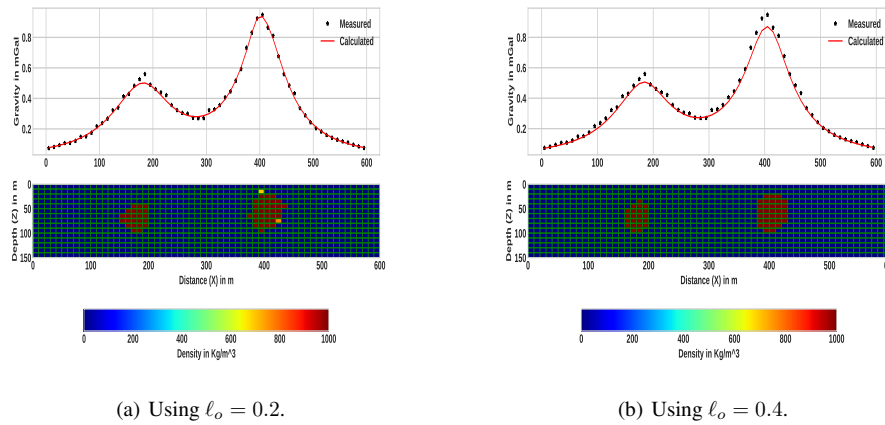
17

(a) Using $\ell_o = 0.2$.

(b) Using $\ell_o = 0.4$.

Figure 4: Inversion results, using different $\ell_o$ values, for the first synthetic model given in Fig. 3(a).

405    upper part. Using the generated synthetic data, the inversion was initiated by assigning an initial zero

406    density to each cell. We set initial $\ell_o = 0.3$. The density contrast limits are bounded between lower

407    bound $\boldsymbol{\rho}_{min} = 0$ and the upper bound $\boldsymbol{\rho}_{max} = 3000 \ kg/m^3$. Even though a maximum iteration of 20

408    was set, the $misfit$ and $smy$ between two consecutive iterations gradually fall below the threshold set

409    after the $14^{th}$ iteration. The total computation time is approximately 15.73 seconds. In Fig. 5(b), the

410    resulting model from the inversion of the second synthetic model (Fig. 5(a)) using the proposed method

411    is presented. As can be seen in Fig. 5(b) upper panel the modeled gravity data (solid line) fits adequately

412    with the synthetic data. The result, presented in Fig. 5(b) lower panel, indicates an acceptable recon-

413    struction of the synthetic multi-sources and multi-shape bodies that are located at different depths. The

414    true shape, location and density of the causative bodies are recovered adequately. Like the first example

415    the reproduced images of the localized multiple sources are compact and sharp (Fig. 5(b) lower panel).

416    For the third and fourth synthetic examples: (I) The subsurface model was discretized into 100 x 20

417    rectangular cells. Each cell has a size of 50 m in X and Z directions. (II) The synthetic gravity data

418    were computed on 100 data points with a sample spacing of 50 m. The third synthetic model includes

419    two dipping dikes in opposite directions. The causative 2-D bodies have different sizes and the same

420    density contrast that amounts to $1000 \ kg/m^3$ in a homogeneous background zero density. The top part

421    of the shallower dipping dike lies at a depth of 200 m and that of the deeper dike at a depth of 250

422    m. The computed gravity anomalies were contaminated by uncorrelated Gaussian noise whose standard

423    deviation was equal to 4% of the difference between the maximum and the minimum anomaly and zero

18
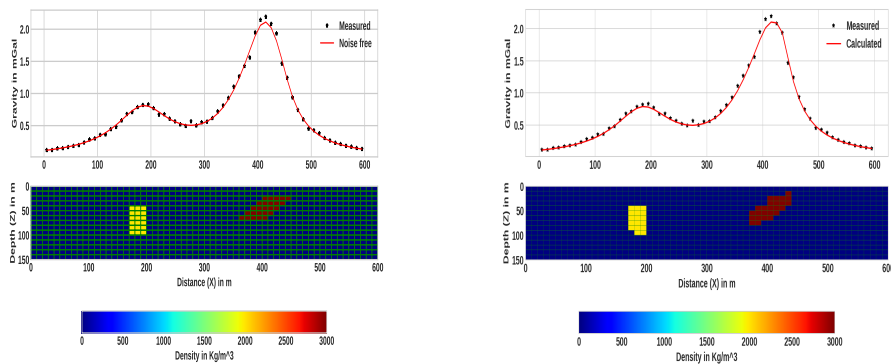
(a) Synthetic model consisting of a dipping dike and vertical rectangular block and the corresponding gravity data.

(b) The density model obtained by inverting the gravity data using the developed method. The predicted data as a result of inversion process are shown on the top panels (solid line).

Figure 5: The second example synthetic model and the corresponding inversion result.

mean. The synthetic model and the corresponding data are shown in Fig. 6 at lower and upper panels respectively.
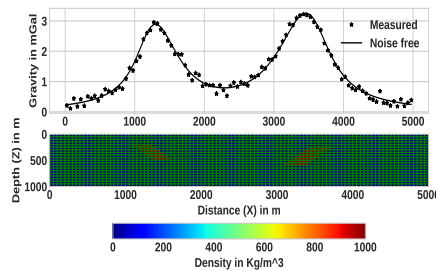


Figure 6: The third synthetic model that comprises two dikes at various depths with the density contrast that amounts to 1000 $kg/m^3$ and the corresponding gravity data.

The inversion process was commenced by setting the densities of all cells to zero. The initial value of $\ell_o$ was set to 0.4. The bounding density ranges were set to a minimum value $\rho_{min} = 0$ and maximum value $\rho_{max} = 1000 \ kg/m^3$. The maximum number of iterations was set to 20. Here, the inversion converged after the $13^{th}$ iteration and the total computation time is approximately 66.49 seconds. The resulting model and the inverted data using the proposed method are shown in Fig. 7(b). For the sake of comparison keeping all inversion parameters the same, the synthetic data was also inverted with the classical L$_2$-norm regularized inversion approach and the obtained result is shown in Fig. 7(a). As it

19

433  can be seen from the lower panel of Fig. 7(b), unlike the model in Fig. 7(a), the developed method was

434  able to produce a compact and sharp model successfully. The other concern, which can be seen from

435  the result in Fig. 7(a), is that the target density contrast values are underestimated in the case of the

436  conventional $L_2$-norm inversion. In contrast, the geometrics, locations, and densities of both anomalous

structures were adequately recovered with the presented inversion method (see Fig. 7(b)).
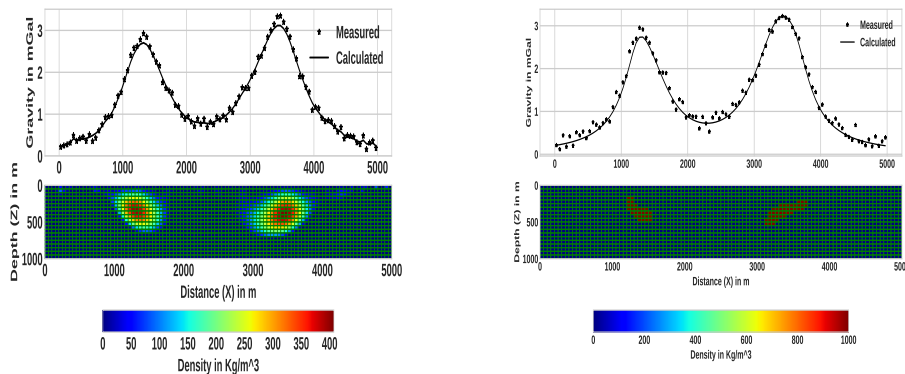


(a) Using the conventional minimum norm ($L_2$-norm) smooth stabilizer and the corresponding data fit.

(b) Using the presented method

Figure 7: Inversion results of the third synthetic example in Fig. 6.

437

438  The fourth synthetic model consists of two different rectangular anomalous bodies (Fig. 8(a) lower

439  panel). The anomalous structures have different dimensions and are buried at different depths. The top

440  of the first rectangular block is placed at a depth of 200 m and its density contrast is -1000 $kg/m^3$ while

441  the top of the second block is placed at a depth of 250 m and has a density contrast of 1000 $kg/m^3$.

442  Different density contrast, size, and depth of adjacent structures have been considered to show the ability

443  of the presented inversion method in reconstructing true parameters for these models. In this synthetic

444  example, the computed anomalies are contaminated by Gaussian noise with a standard deviation of 3%

445  of the difference between the maximum and the minimum anomaly.

446   For the current example, the inversion process was initialized by setting the initial value of $\ell_o$ = 0.5.

447  The lower bound for the density constraint $\rho_{min}$ = -1000 $kg/m^3$ and the upper bound $\rho_{min}$ = 1000

448  $kg/m^3$. Similar to the previous examples, though the maximum number of iterations was set to be 20,

449  the iterative step terminated when the proposed combined criterion is satisfied after 11 iterations. The ap-

450  proximate running time required to finish the inversion is 55.64 seconds. Figure 8(b) lower panel shows

451  the recovered density contrast model. The corresponding fits between synthetic (stars) and predicted
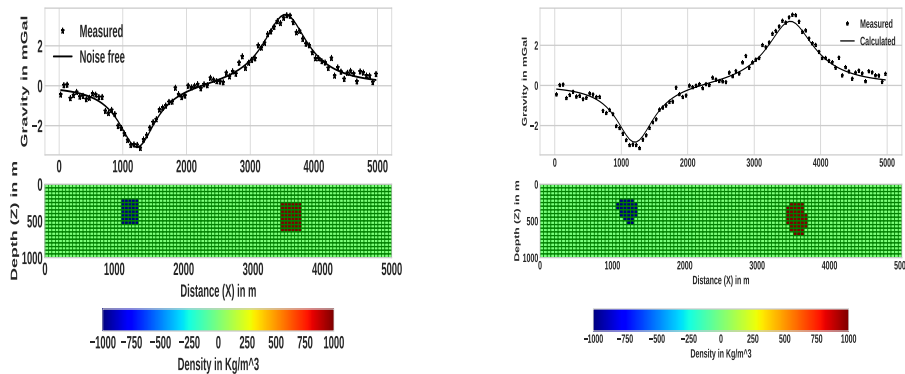
(a) Synthetic model consisting of two rectangular bodies at various depths with different density contrast and the corresponding noise free and contaminated gravity anomalies.

(b) The lower panel shows recovered density contrast model obtained by inverting the gravity data using the developed method, while the upper one shows the associated fits between the synthetic data that is taken from (a) and the predicted response.

Figure 8: The fourth synthetic model example and the corresponding inversion result.

data (line) are shown in the upper panel of the same figure. We can see that the recovered rectangular

bodies are compact and have sharp boundaries. The obtained results also indicate that the depth and

density contrast of the anomalous rectangular bodies have been determined sufficiently.

Here, the effectiveness and the advantage of the proposed combined stopping criterion are illustrated

by comparing it with another commonly used stopping condition. For this reason, the inversion process

was performed again with the developed inversion method using only the misfit function ($|misfit^{k-1} -$

$misfit^k|$) as a stopping condition. Note that, for comparison purposes, all the other inversion parame-

ters are set the same except for the stopping criterion. The resulting recovered density contrast models

and the data fit are presented in Fig. 9. The corresponding values of the $misfit$ and $smy$ as a function

of iteration number are also shown in Fig. 10(a). For the sake of comparison, the $misfit$ and $smy$

when using the proposed combined stopping criterion for the same data set are also presented in Fig.

10(b). The stopping condition $|misfit^{k-1} - misfit^k| \leq \mu$ was reached after 5 iterations, as shown

in the curve of Fig. 10(a) before the true density distribution has been recovered fully. In other words,

the estimated models are not satisfactory because densities lower than the target density are observed

around the edges of the anomalous bodies ( Fig. 9). This indicates that unlike the result presented in

Fig. 8(b), where the proposed combined stopping condition is used, quitting the iterative process only

with $|misfit^{k-1} - misfit^k| \leq \mu$ criterion produces a premature solution that is before the maximum

469 compactness is achieved.

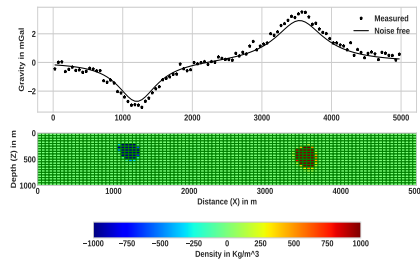A number of other numerical experiments we carried out showed that there are situation where either



Figure 9: Inversion result obtained using only the commonly used criterion ($|misfit^{k-1} - misfit^k|$) and the corresponding data fit (upper panels) for the synthetic example in Fig. 8(a). The obtained density model shows that compact and sharp model is not approximately achieved due to the termination before the iterative procedure has reached convergence.
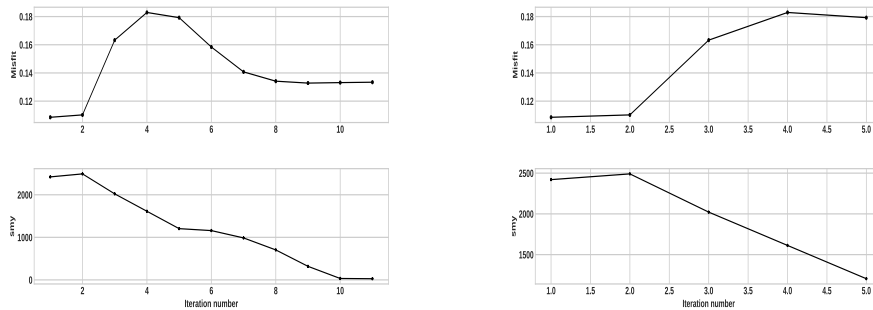


(a) Using the proposed combined stopping condition      (b) Using only $|misfit^{k-1} - misfit^k| \leq \mu$

Figure 10: The progression of $misfit$ and $smy$ in the course of the iteration during the inversion of the fourth example synthetic data.

470

471    $misfit^k|$ or $|misfit^{k-1} - misfit^k|$ fall below the given threshold values, at earlier iterations, before the

472 true density is fully recovered. Thus, it is hard to take only one criterion as a termination condition. As

473 stated in Sect. 2.3.6, it has been mentioned that the same has also be pointed out in number of previous

474 works (Rao et al., 2018). Whereas, in the case of the proposed criterion that is when both the conditions

475    $|smy^{k-1} - smy^k| \leq \tau$ and $|misfit^{k-1} - misfit^k| \leq \mu$ are satisfied at the same time the inversion

476 process yields an acceptable model. This clearly illustrates the advantage of using the proposed stopping

477 criterion and its effectiveness in quitting the iterative scheme after optimal number of iterations. To fur-

478 ther illustrate the effectiveness of the proposed combined criterion, the inversion process is allowed to
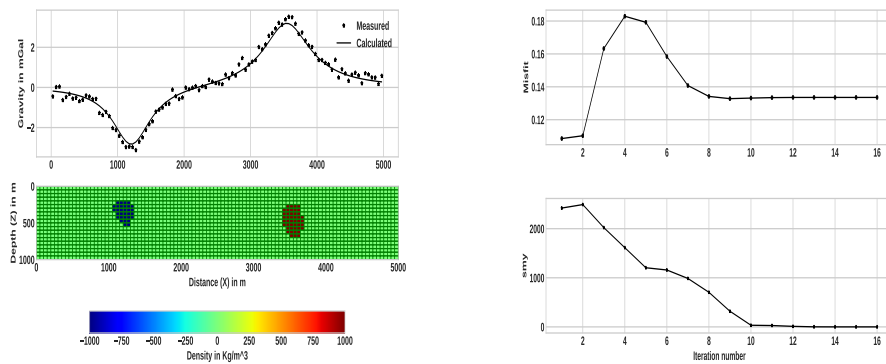
(a) The obtained recovered density model (lower panel) and the corresponding data fit (upper panel).

(b) Progression of $misfit$ (top panel) and $smy$ (lower panel) in the course of the iterative procedure.

Figure 11: Late iteration termination (at $16^{th}$ iteration) inversion result and the corresponding $misfit$ and $smy$ variation with iteration number for the fourth example in Fig 8.

479   continue to the $16^{th}$ iteration and the model as a result of this is presented in Fig. 11(a). The progression

480   of the $misfit$ and $smy$ in the course of the iterative procedure are also given in Fig. 11(b). As it can be

481   seen from the result (Fig. 11(b)) the solution obtained at subsequent iterations, after the $11^{th}$ iteration

482   where the iteration is terminated with the proposed stopping condition, remains virtually unaltered. This

483   can also be observed from the $misfit$ and $smy$ variation curves shown in Fig. 11(b), in such that after

484   $11^{th}$ iteration the $misfit$ and $smy$ values remain literally unchanged. Moreover, the results also indicate

485   the appropriateness of the suggested threshold values $\mu$ and $\tau$ used in the proposed stopping criterion.

486   The other thing one can observe from the results in Fig. 11 is the stability of the developed inversion

487   method. This can also illustrate the effectiveness of the newly proposed auto-adaptive regularization

488   technique (Eq. (18)) and error weighting function (Eq. (16).

489   In general, the presented method was tested with noise contaminated data that are generated from dif-

490   ferent geometries, locations, sizes, and densities contrasts of causative bodies and it has successfully

491   recovered all models. Moreover, all the reconstructed images of the presented synthetic models are

492   compact and sharp. Numerous synthetic data inversions were performed to analyze the impact of the

493   density contrast bounds. The obtained results, which are not presented here, suggest that the values of

494   density contrast bounds have a significant effect on the results, and hence to recover a feasible model a

495   good knowledge of the density bounds is vital. This also pointed out by number of authors, for exam-

496   ple Vatankhah et al. (2017); Li et al. (2018) and Utsugi (2019), in the case of inversion methods that

23

497 use non-smooth stabilizers ($L_1$-norm or $L_0$-norm). Provided that the lower and upper density contrast

498 bounds are chosen properly, this inversion technique produces acceptable solutions. Therefore, as it was

499 demonstrated using synthetic examples, the proposed method has effectively and efficiently recovered

500 the synthetic models. Generally, the tests performed on different geometry synthetic models showed that

501 the method gives acceptable results for localized multi-sources anomalies at different depths with sharp

502 features.

## 4 Real Data Test

504 To test the method in the real world, where the gravity data is contaminated with noise the improved

505 algorithm is implemented on gravity data acquired on different published geologic settings. The first one

506 is taken from Green (1975) by carefully digitizing the residual gravity data. As it was given in Green

507 (1975) the data was measured over the Guichon Creek batholith in south-central British Columbia. For

508 the details about the measurement and geology the reader is referred to Ager et al. (1973) and Ager

509 (1972). The residual gravity profile is digitized at a regular intervals of 0.5 km to produce a total of 64

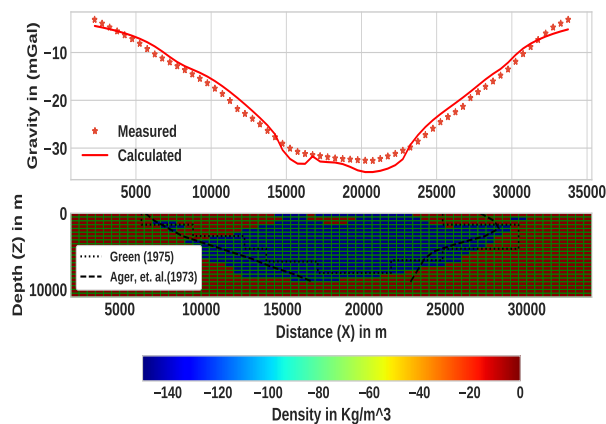data points as shown in Fig. 12. For the inversion, the source volume beneath the anomaly was divided



Figure 12: The observed gravity anomaly over Guichon Creek batholith in south-central British Columbia (after Green (1975)) and its inversion result. Digitized data (star marks) with calculated data (solid line) shown on the top panel. Corresponding recovered density contrast model after 9th iteration shown on the bottom panel. The recovered body density contrast is represented by the color scale bar. For comparison, the results obtained by Ager et al. (1973), which was obtained from drilling and Green (1975) are also presented.

510

511  into 64 x 22 square lattice with dimensions of each cell being 0.5 km in both X and Z-directions. Based

512  on the a prior information from Ager (1972) density values were constrained between the limits $\rho_{min}$

513  = -150 $kg/m^3$ and $\rho_{max}$ = 0.001 $kg/m^3$. We start the inversion with a homogeneous initial model in

514  which every block has the same zero density and an initial $\ell_o$ value of 0.48. The inversion was terminated

515  after 9$^{th}$ iteration because the stopping criteria are fulfilled. The resulting model is presented in Fig. 12.

516  For comparison, the results obtained by Ager et al. (1973) and Green (1975) are also included in Fig.

517  12. The shape, real extent of the anomaly, and depth to bottom from the developed method are very

518  close to the true geological feature (Ager et al., 1973) which was obtained from drilling. That means the

519  implementation of the presented method resulted in a better solution compared Green (1975). Note that,

520  this reasonable result is obtained by using only the density contrast limits as a prior information.

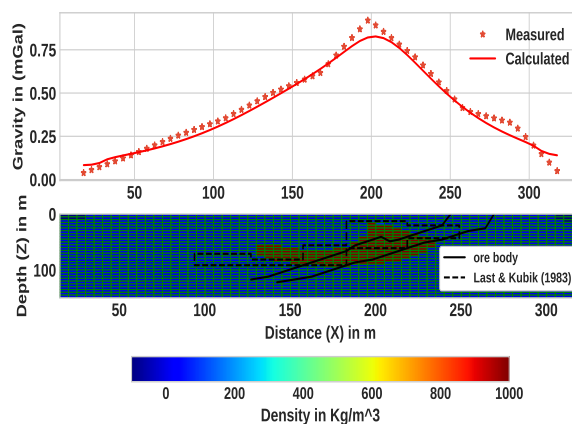The second test on measured gravity data is carried out using the published data by Last & Kubik



Figure 13: An observed gravity anomaly over the Woodlawn ore body, New South Wales (After Last & Kubik (1983)) and the its inversion result. The digitized data (star marks) is shown together with calculated data (solid line) on the top panel. The corresponding recovered density contrast model after 11$^{th}$ iteration shown on bottom panel and the ore body proved by drilling is shown with solid line. The recovered body density contrast is represented by the color scale bar.

521

522  (1983) over the Woodlawn massive sulfide ore body, New South Wales, Australia. The residual anomaly

523  of the area consisting of 61 data measurements, sampled every 5 m, is digitized from Last & Kubik

524  (1983). The details about the data measurement and the geology of the area are discussed in Whiteley

525  (1981). The model subsurface was divided into 61 by 30 blocks with a dimension of 5 m in both X- and

526  Z-direction. Inverse modeling was performed with bounding constraints $\rho_{min} = -600$ and $\rho_{max} = 1000$

25

527 $kg/m^3$. The initial given value for $\ell_o$ is 0.6. The final solution was obtained after the $11^{th}$ iteration. The

528 reconstructed model including the final model of Last & Kubik (1983) are shown in Fig. 13. The cross-

529 section of the ore body verified by drilling (Whiteley, 1981) is also shown in the figure. The recovered

530 model is approximately coincident with the shape, depth of burial and density of the known ore body.

531 Areas of misfits in the current and previous works are believed to be caused by the termination of the

532 original data at both ends before it reaches the background level. Thus, this can be additional evidence

533 that the presented method can be successfully applied to real data.

# 5 Conclusion

535 We have presented an alternative gravity inversion method that can produce compact and sharp images

536 by using the $L_0$-norm stabilizing functional that helps to model geological features with non-smooth,

537 blocky geologic bodies. Physical parameter inequality constraints, and depth weighting are integrated

538 into the procedure. The method also incorporates an auto-adaptive regularization technique, which auto-

539 matically determines a suitable regularization parameter at every iteration, and an error weighting func-

540 tion that helps to improve both the stability and convergence of the method. One of the strongest sides of

541 the proposed auto-adaptive regularization and error weighting matrix is that they are not dependent on a

542 priori knowledge of the noise level. Because of that, the method can yield reasonable results even when

543 the noise level of the data is not known properly. We implemented a combined stopping criteria and

544 illustrated its effectiveness to terminate the iterative inversion process after an optimal number of steps.

545 To illustrate the efficiency and the capacity of the proposed procedure numerous synthetic tests were

546 done. From these, four synthetic examples were presented. According to the results from these syn-

547 thetic examples, the method can be applied for multi-source localized bodies located at different depths

548 and having different geometries with sharp features. Furthermore, the method proved to be efficient in

549 resolving causative bodies both vertically and laterally and produced compact and sharp images. The

550 obtained results also indicate that the method behaves well with different noise levels embedded in the

551 data and still retains its stability. This can confirm the robustness and stability of the developed inversion

552 method for different noise levels. The method was also tested on measured gravity data. We obtained

553 geologically acceptable models and the results showed that our approach is effective and reliable. From

554 a computational point of view, the method is efficient and can be easily run on a personal computer just

555 in a few seconds. In conclusion, the developed method is advantageous in such that it is stable, efficient,

556    and resolves sharp subsurface futures with acceptable resolving capacity.

## Data Availability

The authors confirm that the real data supporting the findings of this study are available within the articles:

1. Green, W. R. (1975) Inversion of gravity profiles by use of a backus-gilbert approach. Geophysics, 40, 763–772 . and its supplementary material.

2. Last, B. and Kubik, K. (1983) Compact gravity inversion. Geophysics, 48, 713–721. and its supplementary material

## Author contributions

MGG developed the methodology; EL supervised the research work; MGG wrote the manuscript draft; EL reviewed and edited the manuscript.

## Competing interests

The authors declare that they have no known competing financial interests or personal relationships that could have appeared to influence the work reported in this paper.

## Acknowledgements

# References

Ager, C., Ulrych, T., & McMillan, W., 1973. A gravity model for the guichon creek batholith, south-central british columbia, *Canadian Journal of Earth Sciences*, **10**(6), 920–935.

Ager, C. A., 1972. *A gravity model for the Guichon Creek Batholith*, Ph.D. thesis, University of British Columbia.

Ajo-Franklin, J., Minsley, B., & Daley, T., 2007. Applying compactness constraints to differential traveltime tomography: Geophysics, 72, *R67–R75*.

Al-Chalabi, M., 1971. Some studies relating to nonuniqueness in gravity and magnetic inverse problems, *Geophysics*, **36**(5), 835–855.

Aster, R. C., Borchers, B., & Thurber, C. H., 2018. *Parameter estimation and inverse problems*, Elsevier.

Barbosa, V. C. F. & Silva, J. B., 1994. Generalized compact gravity inversion, *Geophysics*, **59**(1), 57–68.

Bertete-Aguirre, H., Cherkaev, E., & Oristaglio, M., 2002. Non-smooth gravity problem with total variation penalization functional, *Geophysical Journal International*, **149**(2), 499–507.

Blakely, R. J., 1996. *Potential theory in gravity and magnetic applications*, Cambridge university press.

Borges, L. S., Bazán, F. S. V., & Cunha, M. C., 2015. Automatic stopping rule for iterative methods in discrete ill-posed problems, *Computational and Applied Mathematics*, **34**(3), 1175–1197.

Boulanger, O. & Chouteau, M., 2001. Constraints in 3D gravity inversion, *Geophysical prospecting*, **49**(2), 265–280.

Camacho, A. G., Montesinos, F. G., & Vieira, R., 2002. A 3-D gravity inversion tool based on exploration of model possibilities, *Computers & Geosciences*, **28**(2), 191–204.

Camacho, A. G., Fernández, J., & Gottsmann, J., 2011. A new gravity inversion method for multiple subhorizontal discontinuity interfaces and shallow basins, *Journal of Geophysical Research: Solid Earth*, **116**(B2).

Cella, F. & Fedi, M., 2012. Inversion of potential field data using the structural index as weighting function rate decay, *Geophysical Prospecting*, **60**(2), 313–336.

600  Commer, M., 2011.  Three-dimensional gravity modelling and focusing inversion using rectangular
601      meshes, *Geophysical Prospecting*, **59**(5), 966–979.

602  Ekinci, Y. L., 2008.  2D focusing inversion of gravity data with the use of parameter variation as a
603      stopping criterion, *Journal of the Balkan geophysical society*, **11**(1), 1–9.

604  Farquharson, C. G., 2008.  Constructing piecewise-constant models in multidimensional minimum-
605      structure inversions, *Geophysics*, **73**(1), K1–K9.

606  Farquharson, C. G. & Oldenburg, D. W., 2004. A comparison of automatic techniques for estimating the
607      regularization parameter in non-linear inverse problems, *Geophysical Journal International*, **156**(3),
608      411–425.

609  Fei, Z., Chunhui, T., Tao, W., Zhaofa, Z., & Cai, L., 2018. 3D focused inversion of near-bottom magnetic
610      data from autonomous underwater vehicle in rough seas, *Ocean Science Journal*, **53**(2), 405–412.

611  Feng, X., Liu, S., Guo, R., Wang, P., & Zhang, J., 2020.  Gravity inversion of blocky basement relief
612      using $L_0$-norm constraint with exponential density contrast variation, *Pure and Applied Geophysics*,
613      **177**(8), 3913–3927.

614  Fournier, D., Heagy, L. J., & Oldenburg, D. W., 2020.  Sparse magnetic vector inversion in spherical
615      coordinatessparse magnetic vector inversion, *Geophysics*, **85**(3), J33–J49.

616  Gebre, M. G. & Lewi, E., 2022.  L0-norm gravity inversion with new depth weighting function and
617      bound constraints, *Acta Geophysica*, **70**(4), 1619–1634.

618  Ghalehnoee, M. H., Ansari, A., & Ghorbani, A., 2017.  Improving compact gravity inversion based on
619      new weighting functions, *Geophysical Journal International*, **208**(1), 546–560.

620  Gholami, A. & Aghamiry, H. S., 2017.  Iteratively re-weighted and refined least squares algorithm for
621      robust inversion of geophysical data, *Geophysical Prospecting*, **65**(S1), 201–215.

622  Grandis, H. & Dahrin, D., 2014.  Constrained two-dimensional inversion of gravity data, *Journal of
623      Mathematical and Fundamental Sciences*, **46**(1), 1–13.

624  Green, W. R., 1975.  Inversion of gravity profiles by use of a Backus-Gilbert approach, *Geophysics*,
625      **40**(5), 763–772.

626 Guillen, A. & Menichetti, V., 1984. Gravity and magnetic inversion with minimization of a specific

627    functional, *Geophysics*, **49**(8), 1354–1360.

628 Hinze, W. J., Von Frese, R. R., Von Frese, R., & Saad, A. H., 2013. *Gravity and magnetic exploration:*

629    *principles, practices, and applications*, Cambridge University Press.

630 Last, B. & Kubik, K., 1983. Compact gravity inversion, *Geophysics*, **48**(6), 713–721.

631 Lelièvre, P. G., Oldenburg, D. W., & Williams, N. C., 2009. Integrating geological and geophysical data

632    through advanced constrained inversions, *Exploration Geophysics*, **40**(4), 334–341.

633 Lelievre, P. G., Farquharson, C. G., & Bijani, R., 2015. 3d potential field inversion for wireframe surface

634    geometry, in *2015 SEG Annual Meeting*, OnePetro.

635 Levin, E. & Meltzer, A. Y., 2017. Stopping criterion for iterative regularization of large-scale ill-posed

636    problems using the Picard parameter, *arXiv preprint arXiv:1707.04200*.

637 Lewi, E., 1997. *Modelling and inversion of high precision gravity data*, Ph.D. thesis, Verlag der Bay-

638    erischen Akademie der Wissenschaften, Munchen, Germany, ISSN 0065 -5325, ISBN3769695119.

639 Li, F., Xie, R., Song, W., Zhao, T., & Marfurt, K., 2017. Optimal $L_q$-norm regularization for sparse

640    reflectivity inversion, in *SEG Technical Program Expanded Abstracts 2017*, pp. 677–681, Society of

641    Exploration Geophysicists.

642 Li, Y. & Oldenburg, D. W., 1996. 3-D inversion of magnetic data, *Geophysics*, **61**(2), 394–408.

643 Li, Y. & Oldenburg, D. W., 1998. 3-D inversion of gravity data, *Geophysics*, **63**(1), 109–119.

644 Li, Y. & Oldenburg, D. W., 2003. Fast inversion of large-scale magnetic data using wavelet transforms

645    and a logarithmic barrier method, *Geophysical Journal International*, **152**(2), 251–265.

646 Li, Z. & Yao, C., 2020. 3D sparse inversion of magnetic amplitude data when strong remanence exists,

647    *Acta Geophysica*, pp. 1–11.

648 Li, Z., Yao, C., Zheng, Y., Wang, J., & Zhang, Y., 2018. 3D magnetic sparse inversion using an interior-

649    point method, *Geophysics*, **83**(3), J15–J32.

650 Meng, Z., 2016. 3D inversion of full gravity gradient tensor data using SL0 sparse recovery, *Journal of*

651    *Applied Geophysics*, **127**, 112–128.

652    Meng, Z.-H., Xu, X.-C., & Huang, D.-N., 2018. Three-dimensional gravity inversion based on sparse

653    recovery iteration using approximate zero norm, *Applied Geophysics*, **15**(3-4), 524–535.

654    Menke, W., 1989. *Geophysical data analysis: Discrete inverse theory*, International Geophysics Series,

655    New York: Academic Press.

656    Nagy, D., 1966. The gravitational attraction of a right rectangular prism, *Geophysics*, **31**(2), 362–371.

657    Paoletti, V., Ialongo, S., Florio, G., Fedi, M., & Cella, F., 2013. Self-constrained inversion of potential

658    fields, *Geophysical Journal International*, **195**(2), 854–869.

659    Peng, G. & Liu, Z., 2021. 3D inversion of gravity data using reformulated $L_p$-norm model regularization,

660    *Journal of Applied Geophysics*, **191**, 104378.

661    Pilkington, M., 2008. 3D magnetic data-space inversion with sparseness constraints, *Geophysics*, **74**(1),

662    L7–L15.

663    Portniaguine, O. & Zhdanov, M. S., 1999. Focusing geophysical inversion images, *Geophysics*, **64**(3),

664    874–887.

665    Rao, K., Malan, P., & Perot, J. B., 2018. A stopping criterion for the iterative solution of partial differ-

666    ential equations, *Journal of Computational Physics*, **352**, 265–284.

667    Rezaie, M. & Moazam, S., 2017. A new method for 3-D magnetic data inversion with physical bound,

668    *Journal of Mining and Environment*, **8**(3), 501–510.

669    Rezaie, M., Moradzadeh, A., Kalate, A. N., & Aghajani, H., 2017. Fast 3D focusing inversion of gravity

670    data using reweighted regularized Lanczos bidiagonalization method, *Pure and Applied Geophysics*,

671    **174**(1), 359–374.

672    Silva, J. B. & Barbosa, V. C., 2006. Interactive gravity inversion, *Geophysics*, **71**(1), J1–J9.

673    Silva, J. B., Medeiros, W. E., & Barbosa, V. C., 2001. Potential-field inversion: Choosing the appropriate

674    technique to solve a geologic problem, *Geophysics*, **66**(2), 511–520.

675    Singh, A., Sharma, S. P., Akca, İ., & Baranwal, V. C., 2018. Fuzzy constrained $L_p$-norm inversion of

676    direct current resistivity data, *Geophysics*, **83**(1), E11–E24.

677  Stocco, S., Godio, A., & Sambuelli, L., 2009. Modelling and compact inversion of magnetic data: A

678  matlab code, *Computers & Geosciences*, **35**(10), 2111–2118.

679  Sun, J. & Li, Y., 2014. Adaptive $L_p$ inversion for simultaneous recovery of both blocky and smooth

680  features in a geophysical model, *Geophysical Journal International*, **197**(2), 882–899.

681  Tikhonov, A. N., Goncharsky, A., Stepanov, V., & Yagola, A. G., 2013. *Numerical methods for the*

682  *solution of ill-posed problems*, vol. 328, Springer Science & Business Media.

683  Utsugi, M., 2019. 3-d inversion of magnetic data based on the $L_1$-$L_2$-norm regularization, *Earth, Planets*

684  *and Space*, **71**(1), 1–19.

685  Varfinezhad, R., Oskooi, B., & Fedi, M., 2020. Joint inversion of dc resistivity and magnetic data,

686  constrained by cross gradients, compactness and depth weighting, *Pure and Applied Geophysics*,

687  **177**(9), 4325–4343.

688  Varfinezhad, R., Fedi, M., & Milano, M., 2022. The role of model weighting functions in the gravity

689  and dc resistivity inversion, *IEEE Transactions on Geoscience and Remote Sensing*, **60**, 1–15.

690  Vatankhah, S., Ardestani, V. E., & Renaut, R. A., 2014. Automatic estimation of the regularization

691  parameter in 2d focusing gravity inversion: application of the method to the safo manganese mine in

692  the northwest of Iran, *Journal of Geophysics and Engineering*, **11**(4), 045001.

693  Vatankhah, S., Renaut, R. A., & Ardestani, V. E., 2017. 3-D projected $L_1$ inversion of gravity data us-

694  ing truncated unbiased predictive risk estimator for regularization parameter estimation, *Geophysical*

695  *Journal International*, **210**(3), 1872–1887.

696  Virtanen, P., Gommers, R., Oliphant, T. E., Haberland, M., Reddy, T., Cournapeau, D., Burovski, E.,

697  Peterson, P., Weckesser, W., Bright, J., et al., 2020. Scipy 1.0: fundamental algorithms for scientific

698  computing in python, *Nature methods*, **17**(3), 261–272.

699  Vogel, C. R., 2002. *Computational methods for inverse problems*, vol. 23, Siam.

700  Wang, Y. & Ma, S., 2007. Projected Barzilai-Borwein method for large-scale nonnegative image restora-

701  tion, *Inverse Problems in Science and Engineering*, **15**(6), 559–583.

702  Whiteley, R. J., 1981. *Geophysical Case Study of the Woodlawn Orebody, New South Wales, Australia:*

703  *The First Publication of Methods and Techniques Tested Over a Base Metal Orebody of the Type*

704     *which Yields the Highest Rate of Return on Mining Investment with Modest Capital Requirements.*

705     *Maps*, Pergamon.

706     Zhao, C., Yu, P., & Zhang, L., 2016. A new stabilizing functional to enhance the sharp boundary in

707      potential field regularized inversion, *Journal of Applied Geophysics*, **135**, 356–366.

708     Zhdanov, M. & Tolstaya, E., 2004. Minimum support nonlinear parametrization in the solution of a 3D

709      magnetotelluric inverse problem, *Inverse problems*, **20**(3), 937.

710     Zhdanov, M. S., 2002. *Geophysical inverse theory and regularization problems*, vol. 36, Elsevier.

711     Zhdanov, M. S., 2009. New advances in regularized inversion of gravity and electromagnetic data,

712      *Geophysical Prospecting*, **57**(4), 463–478.

# Figure Captions

Figure 1. A 2-D model of the subsurface under a gravity profile. Gravity stations ($X_i$) are located at the centers of the blocks, indicated by the $\bigtriangledown$ symbols.

Figure 2. Comparison of the minimum support stabilizing function for different values of $\varepsilon$.

Figure 3. The first synthetic model and the result of the inversion.

Figure 4. Inversion results, using different $\ell_o$ values, for the first synthetic model given in Fig. 3(a).

Figure 5. The second example synthetic model and the corresponding inversion result.

Figure 6. The third synthetic model that comprises two dikes at various depths with the density contrast that amounts to 1000 $kg/m^3$ and the corresponding gravity data

Figure 7. Inversion results of the third synthetic example in Fig. 6.

Figure 8. The fourth synthetic model example and the corresponding inversion result.

Figure 9. Inversion result obtained using only the commonly used criterion ($|misfit^{k-1} - misfit^k|$) and the corresponding data fit (upper panels) for the synthetic example in Fig. 8(a). The obtained density model shows that compact and sharp model is not approximately achieved due to the termination before the iterative procedure has reached convergence.

Figure 10. The progression of $misfit$ and $smy$ in the course of the iteration during the inversion of the fourth example synthetic data.

Figure 11. Late iteration termination (at $16^{th}$ iteration) inversion result and the corresponding $misfit$ and $smy$ variation with iteration number for the fourth example in Fig. 8(a).

Figure 12. The observed gravity anomaly over Guichon Creek batholith in south-central British Columbia (after Green 1975) and its inversion result. Digitized data (star marks) with calculated data (solid line) shown on the top panel. Corresponding recovered density contrast model after $9^{th}$ iteration shown on the bottom panel. The recovered body density contrast is represented by the color scale bar. For comparison, the results obtained by Ager (1973), which was obtained from drilling and Green (1975) are also presented.

739     Figure 13. An observed gravity anomaly over the Woodlawn ore body, New South Wales (After

740     Last and Kubik (1983)) and the its inversion result. The digitized data (star marks) is shown

741     together with calculated data (solid line) on the top panel. The corresponding recovered density

742     contrast model after 11th iteration shown on bottom panel and the ore body proved by drilling is

743     shown with solid line. The recovered body density contrast is represented by the color scale bar